ACS APPLIED MATERIALS & INTERFACES

Research Article

www.acsami.org

Acidity-Triggered Tumor Retention/Internalization of Chimeric Peptide for Enhanced Photodynamic Therapy and Real-Time Monitoring of Therapeutic Effects

Kai Han,*[,†] Wei-Yun Zhang,[†] Zhao-Yu Ma,[†] Shi-Bo Wang,[‡] Lu-Ming Xu,[§] Jia Liu,[§] Xian-Zheng Zhang,[‡] and He-You Han*[,†]

[†]State Key Laboratory of Agricultural Microbiology, College of Science, Huazhong Agricultural University, Wuhan 430070, China

[‡]Key Laboratory of Biomedical Polymers of Ministry of Education & Department of Chemistry, Wuhan University, Wuhan 430072, China

[§]China Research Center for Tissue Engineering and Regenerative Medicine, Union Hospital, Tongji Medical College, Huazhong University of Science and Technology, Wuhan 430022, China

S *Supporting Information*

ABSTRACT: Photodynamic therapy (PDT) holds great promise in tumor treatment. Nevertheless, it remains highly desirable to develop easy-to-fabricated PDT systems with improved tumor accumulation/internalization and timely therapeutic feedback. Here, we report a tumor-acidity-responsive chimeric peptide for enhanced PDT and noninvasive real-time apoptosis imaging. Both in vitro and in vivo studies revealed that a tumor mildly acidic microenvironment could trigger rapid protonation of carboxylate anions in chimeric peptide, which led to increased ζ potential, improved hydrophobicity, controlled size enlargement, and precise morphology switching from sphere to spherocylinder shape of the chimeric peptide. All of these factors realized superfast accumulation and prolonged retention in the tumor region, selective cellular internalization, and enhanced PDT against the tumor. Meanwhile, this chimeric peptide could further generate reactive oxygen species and initiate cell apoptosis during PDT. The subsequent formation of caspase-3 enzyme hydrolyzed the chimeric peptide, achieving a high signal/noise ratio and timely fluorescence feedback. Importantly, direct utilization of the acidity responsiveness of a biofunctional Asp−Glu−Val−Asp−Gly (DEVDG, caspase-3 enzyme substrate) peptide sequence dramatically simplified the preparation and increased the performance of the chimeric peptide furthest.

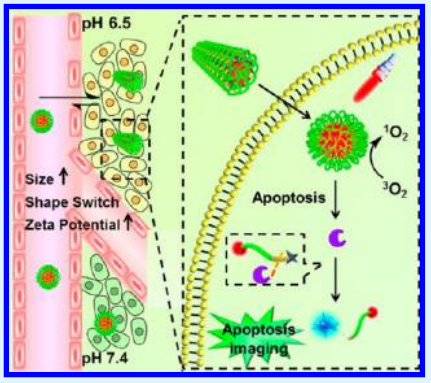

KEYWORDS: *tumor target, acidity-triggered morphology switch, apoptosis imaging, photodynamic therapy, chimeric peptide*

1. INTRODUCTION

Photodynamic therapy (PDT) has obtained considerable attention during the last decades because of negligible drug resistance, precisely controllable phototoxicity, and noninvasiveness to normal tissues.[1−3] Despite the great success of PDT, the further development of PDT is still facing great challenges mainly including disappointed tumor retention/internalization and retarded feedback of the therapeutic effect.[4,5] Generally, nanoparticles designed for accumulation in the tumor region after intravenous (i.v.) injection are strongly dependent on the enhanced permeability and retention (EPR) effect.[6−8] However, the EPR effect is a passive mechanism of tumor accumulation.[9,10] Nanoparticles with small size can still be free of diffusion in the defective vasculature of the tumor tissue and reenter the blood circulation system, which encounters metabolic clearance and compromises targeting efficacy inevitably. A promising approach to solving this limitation is to develop nanoparticles featuring tumor microenvironment-triggered size enlargement to achieve "active" tumor accumulation.[11−14] These nanoparticles can undergo degradation of certain chemical structures under tumor microenvironment stimuli such as acidity, enzymes, or temperature variation.[15−17] Consequently, the packing parameter (P) of nanoparticles changed, leading to hydrodynamic size enlargement, which can mechanically restrict passive diffusion of biosubstances in vascular architecture with high efficacy. Unfortunately, the degradation of certain chemical structures under stimuli is time-consuming, which increases the risk of metabolic clearance of nanoparticles. Even worse, the ratio of hydrophilic and hydrophobic segments cannot be precisely manipulated. Uncontrolled aggregation with sizes up to dozens of micrometers may form. Although it prolongs tumor retention, subsequent cellular internalization can be severely restricted. It is known that other physicochem-

Received: March 29, 2017
Accepted: April 26, 2017
Published: April 26, 2017

DOI: 10.1021/acsami.7b04447
ACS Appl. Mater. Interfaces 2017, 9, 16043−16053

Scheme 1. Schematic Illustration of the Chimeric Peptide for Enhanced PDT and Real-Time Apoptosis Imaging[a]

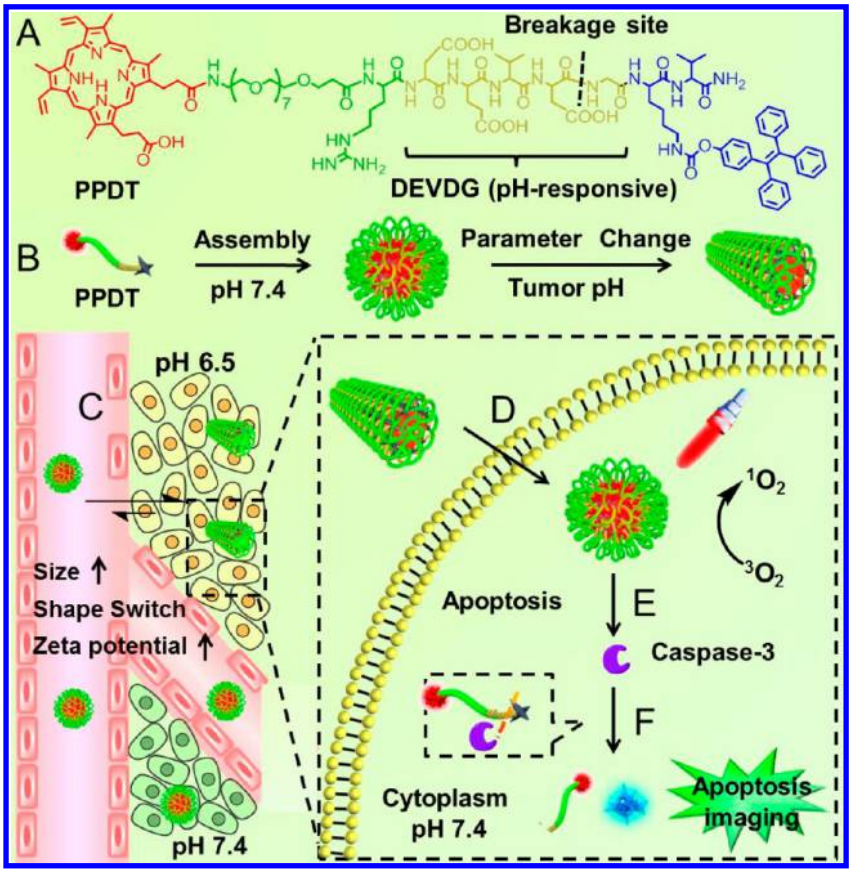

[a](A) The chemical structure of PPDT; (B) self-assembly of PPDT with different pH values; (C) i.v. injection of PPDT and tumor mildly acidic environment-triggered size enlargement and enhanced tumor accumulation; (D) morphology switching and increased ζ-potential-mediated accelerated cellular uptake of PPDT; (E) PDT-induced cell apoptosis; (F) hydrolysis of the DEVDG peptide sequence and AIE-mediated real-time apoptosis imaging.

ical parameters including the surface chemistry and morphology also affect tumor retention and internalization. It can be imagined that if the tumor microenvironment can rationally trigger changes of several physicochemical parameters simultaneously, and not just size enlargement, a promising drug-delivery system with balanced tumor retention and cellular internalization can be expected.

On the other hand, real-time tracking of the biological response of PDT noninvasively should also be considered in order to avoid repeated doses. Traditional evaluation of the PDT efficacy is always dependent on measurement of the tumor volume change, which is generally much delayed.[18,19] Although the apoptosis imaging technique shows great potential in monitoring the biological response of the tumor at an early stage and PDT can initiate cell apoptosis.[20−22] little work has been done to timely evaluate the PDT efficacy via apoptosis imaging, partly because of the fact that most of these apoptosis imaging works rely on a fluorescence resonance energy-transfer (FRET) technique. Both donor and acceptor molecules are required to conjugate at the terminal of specific linkers with optimized spatial distance and spectral overlap to ensure well FRET efficacy, which undoubtedly makes the preparation arduous.

Keeping all of these issues in mind, we developed a very simple but effective acidity-responsive chimeric peptide for superfast tumor accumulation and improved internalization and real-time apoptosis imaging simultaneously. This chimeric peptide bears hydrophobic protoporphyrin IX (PpIX) and aggregation-induced emission (AIE) molecular tetraphenylethylene (TPE) at the terminal of the hydrophilic PEG_8−Arg−DEVDG (Asp−Glu−Val−Asp−Gly) sequence. The obtained chimeric peptide PpIX−PEG_8−RDEVDG−K(TPE)−V−$CONH_2$ was thus designated as PPDT. As shown in Scheme 1, amphiphilic PPDT could self-assemble into spherical nanoparticles at physiological conditions (pH 7.4). Once it arrived at the mildly acidic tumor region, the hydrophilic carboxylate anion in PPDT rapidly got protonated to form hydrophobic carboxylic acid groups (Figure S1).[23−28] This simple and fast protonation process increased the ζ potential and hydrodynamic size and mediated controlled sphere-to-spherocylinder morphology switching of PPDT simultaneously, which realized superfast tumor accumulation and facilitated cellular internalization. After entering the tumor cells, PDT under light irradiation could initiate cell apoptosis. The subsequently emerged caspase-3 enzyme specifically cleaved the DEVDG substrate sequence and liberated the TPE molecule, leading to noninvasively and timely AIE-mediated apoptosis imaging.

2. EXPERIMENTAL SECTION

2.1. Materials. Protoporphyrin IX (PpIX) and 2′,7′-dichlorofluorescein diacetate (DCFH-DA) were obtained from Aladdin Reagent Co. Ltd. (China). Diisopropylethylamine (DIEA), *N*-fluorenyl-9-methoxycarbonyl (FMOC)-protected L-amino acids, trifluoroacetic

DOI: 10.1021/acsami.7b04447
ACS Appl. Mater. Interfaces 2017, 9, 16043−16053

acid (TFA), rink amide resin (loading = 0.51 mmol/g), piperdine, and *o*-benzotriazole-*N*,*N*,*N*′,*N*′-tetramethyluronium hexafluorophosphate (HBTU) were provided by GL Biochem Ltd. (China). FMOC-PEG_8-COOH was purchased from Qian Cheng Technology Co., Ltd. (China). Caspase-3 enzyme was purchased from Biovision. 3-(4,5-Dimethylthiazol-2-yl)-2,5-diphenyltetrazolium-bromide (MTT), fetal bovine serum (FBS), and penicillin−streptomycin were purchased from Pierce. Other reagents were used as received (analytical grade).

2.2. Synthesis of TPE-COOH, PPDT, and PPST. TPE-COOH was synthesized as given in a previous report.[29] PPDT and PPST were synthesized according to the solid-phase peptide synthesis (SPPS) method.[30,31] Briefly, peptide was conjugated to rink amide resin (0.1 g, 0.6 mmol/g) with the help of HBTU/DIEA for 2 h. The FMOC protecting group was deprotected by 20% piperdine/*N*,*N*-dimethylformamide (DMF; v/v) two times (10 + 10 min). The MTT protecting group was selectively moved with 1% TFA in dichloromethane (10 × 5 min). The peptide-loaded resin was treated with a cleavage cocktail (5 mL) of TFA, triisopropylsilane, and H_2O (volume ratio = 95:2.5:2.5) for 2 h. The solution was dropped in ether. Then peptide was precipitated and dried in a vacuum. The molecular weight was characterized via electrospray ionization (ESI-MS).

2.3. Size and Morphology Observation. PPDT was dissolved in a phosphate-buffered saline (PBS) buffer (pH 7.4, 0.5 mM), and the morphology of 50 mg/L PPDT was observed by transmission electron microscopy (TEM; via a JEM-2100 microscope). For morphology observation at pH 6.5, PPDT was dissolved in a PBS buffer (pH 7.4) and then dispersed in the appropriate acidic water to keep the final pH at 6.5. Subsequently, the sample was immediately observed via TEM. The hydrodynamic particle size of 50 mg/L PPDT was detected by a Nano-ZS ZEN3600 instrument. For the pH response time test, PPDT (50 mg/L) at pH 7.4 was added with the appropriate HCl solution (0.01 mol/L) in order to rapidly adjust the pH to 6.5. Then the hydrodynamic particle size was recorded at preset times.

2.4. Reactive Oxygen Species (ROS) Generation. DCFH-DA was used to detect the generation of ROS. Briefly, 30 μL of DCFH-DA was pretreated with NaOH and subsequently mixed with 30 μL of PPDT. The final concentrations of DCFH-DA and PPDT were 5 and 50 mg/L, respectively. The sample was irradiated for preset times by a light-emitting diode (LED; 630 nm). Fluorescence spectra were determined (excitation wavelength = 488 nm). PpIX with equal concentration [12.4 mg/L in 0.5% dimethyl sulfoxide (DMSO)] was used as the negative control.

2.5. Critical Micelle Concentration (cmc) Measurement. The cmc value was determined using pyrene as a sensor.[32] Briefly, various concentrations of PPDT (pH 7.4 or 6.5) were mixed with pyrene (6×10^{-7} mol/L). The fluorescence spectra were determined (emission wavelength = 390 nm; excitation spectra range = 300−360 nm). The change of the intensity ratio of the third and first vibronic bands (I_3/I_1) was plotted against the logarithm of peptide concentrations to determine the critical micelle concentration.

2.6. Caspase-3 Enzymatic Response of PPDT. PPDT (50 mg/L) was incubated with a caspase-3 enzyme solution (1 U/mL, 0.1% 3-[(3-cholamidopropyl)dimethylammonio]-1-propanesulfonate, 50 mM *N*-(2-hydroxyethyl)piperazine-*N*′-(2-ethanesulfonic acid), pH 7.2, dithiothreitol, 10 mM ethylenediaminetetraacetic acid, 50 mM NaCl, and 5% glycerol). The fluorescence spectra were detected at preset times. TPE was excited at 330 nm. To test the sensitivity of caspase-3 enzyme, 50 mg/L PPDT was mixed with various concentrations of caspase-3 enzyme. Fluorescence spectra at 1 min were measured.

2.7. pH-Responsive Cell Internalization. HeLa cells were seeded at an initial density of 1×10^5 cells/well. The culture medium was substituted by PPDT (40 mg/L) in Dulbecco's modified Eagle's medium (DMEM) including 10% FBS at pH 7.4 and 6.5, respectively. A total of 4 h later, the medium with PPDT was removed, and cells were washed with PBS repeatedly. Samples were imaged via confocal laser scanning microscopy (CLSM).

2.8. Endocytosis Pathway Analysis. HeLa cells were seeded at an initial density of 1×10^5 cells/well. Thereafter, HeLa cells were incubated with the endocytosis inhibitors genistein (15 mg/L, inhibitor of caveolin-mediated endocytosis) and amiloride (133 mg/L, inhibitor of macropinocytosis) for 30 min at 37 °C. Then the medium was removed, and PPDT (40 mg/L) in a complete medium with corresponding concentrations of inhibitors at pH 7.4 and 6.5 was added. Besides, to evaluate whether the endocytosis process was energy-dependent, PPDT was added to the HeLa cells and then incubated at 4 °C. A total of 4 h later, all samples were analyzed via flow cytometry.

2.9. PDT-Induced Apoptosis Imaging. HeLa cells were seeded in a six-well plate for 24 h. Then the medium was substituted by PPDT (50 mg/L) in a fresh medium. A total of 4 h later, PPDT was replaced by DMEM with 10% FBS and irradiated by LED for preset times (0, 75, and 150 s). Samples were cultured for another 24 h. Then cells were repeatedly washed for CLSM imaging. Fluorescence imaging was conducted with a filter set (Ex, 405 nm; Em band-pass, 450−500 nm) for TPE and another filter set (Ex, 488 nm; Em band-pass, 550−650 nm) for PpIX.

2.10. In Vitro Cytotoxicity Assay. The cytotoxicity of PPDT against HeLa cells in vitro was tested through MTT assay. After incubation for 24 h on a 96-well plate, various concentrations of PPDT at pH 7.4 or 6.5 were added to incubate with the HeLa cells. Then the medium was replaced by a fresh medium, and 4 h later cells were irradiated by LED for 75 s (29.8 mW/cm^2, 630 nm). Cells were incubated for 48 h, and 20 μL of MTT in a PBS buffer was added. Then the medium was changed with 200 μL of DMSO after 4 h. The absorbance at 490 nm was determined. The percentage of survival cells per the total of nontreated cells was defined as the cell viability. All data were averaged from eight independent experiments. The phototoxicity of PPDT at pH 7.4 with different time irradiations was determined in a similar way.

2.11. In Vivo Tumor Accumulation Imaging, Tissue Distributions, Pharmacokinetic Study. Animal experiments in vivo were tested according to guidelines established by the Huazhong Agricultural University. A H22 tumor model was established by the subcutaneous injection of H22 cells. Mice were intravenously injected with PPDT and PPST solutions via a tail vein (16.15 mg/kg per mouse for PPDT and 15.45 mg/kg per mouse for PPST). For tumor accumulation imaging, at preset times after injection, mice were anesthetized and imaged via a small animal imaging system at the Center for Instrumental Analysis and Metrology (Institute of Virology, Chinese Academy of Sciences). For the tissue distribution study, mice were sacrificed, and various tissues and tumor were exfoliated and imaged at the 24th h after in vivo injection. For the pharmacokinetic study, serum samples of mice were obtained at the time points of 0.5, 2, 4, 6, 8, 10, and 12 h. A PBS buffer was added to dilute them, and repeated freeze−thaw cycles were used to lyse the cells. Furthermore, a 5 min ultrasound was performed, and the solution was centrifuged for 3 min. The fluorescence of the supernatant was measured to determine the amounts of the samples (Ex, 409 nm; Em, 630 nm).

2.12. In Vivo Antitumor Study. H22 cells (ca. 1×10^6 cells/mouse) were injected into mice. Mice were divided into four groups randomly (four mice per group). When tumors reached the approximate size of 100 mm^3, 100 μL of a PBS buffer, PPDT (two groups: with or without light irradiation), and PPST were injected into the mice every other day. PPDT and PPST were 16.15 and 15.45 mg/kg per mouse, respectively. A total of 6 h later, the PPST group and one PPDT group received 220 mW/cm^2 light irradiation for 10 min (laser wavelength = 630 nm), and another PPDT group received no light irradiation. The tumor size as well as mice weight were recorded every day. The tumor volume was defined as V = [(tumor length)(tumor width)^2]/2. The relative tumor volume was defined as V/V_0 (V_0 was the tumor volume at the first day). The relative body weight was defined as M/M_0 (M_0 was the body weight on the first day). When the treatment was finished, the physiological morphology of various tissues was further determined via hematoxylin and eosin (H&E) staining.

2.13. In Vivo Systemic Toxicity. After the treatment was finished, blood samples of various groups were collected. Blood samples were solidified, and supernatant serum was obtained by centrifugation (1600 rpm for 4 min). The amounts of GPT, AST, A/G, TP, BUN,

DOI: 10.1021/acsami.7b04447
ACS Appl. Mater. Interfaces 2017, 9, 16043−16053

and UN were detected at Union Hospital (Tongji Medical College, Wuhan, China) with a Beckman Coulter 5831 biochemistry analyzer.

2.14. Statistical Analysis. Statistical analysis was determined via the Student's *t* test. When the *p* value was below 0.05, the differences were statistically significant.

3. RESULTS AND DISCUSSION

3.1. Synthesis and Characterization of the Chimeric Peptide. PPDT was obtained through a standard fluorenylmethyloxycarbonyl SPPS method, and a detailed synthesis process was performed (Figure S1). The validity of PPDT was confirmed via ESI-MS (for $[M + 2H]^{2+}$, m/z 1136.9; Figure S2). The UV−vis spectrum illustrated that, different from free aggregated PpIX with broadened split bands (at 357 and 443 nm), a Soret band at around 390 nm appeared in PPDT (Figure 1A), indicating negligible aggregation of PPDT at physiological pH.[33,34] Negligible aggregation of PPDT would facilitate PpIX in the ground state to absorb photons and keep them in an excited triplet state, which was in favor of ROS generation.[35] To verify this, ROS generation under light irradiation was investigated using DCFH-DA as a ROS sensor because ROS could rapidly oxidize DCFH-DA and generate 2′,7′-dichlorofluorescein with green fluorescence. As expected, the green fluorescence increment in the PPDT group was obviously higher than that in the PpIX group at preset times (Figure 1B).

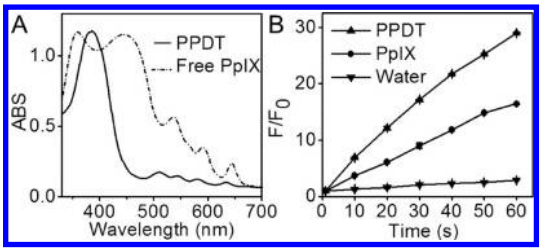

Figure 1. (A) UV−vis spectra of PPDT and PpIX. (B) ROS generation of PPDT with different irradiation times that was measured by the fluorescence spectrum. Free PpIX was dissolved in 0.5% DMSO (negative control).

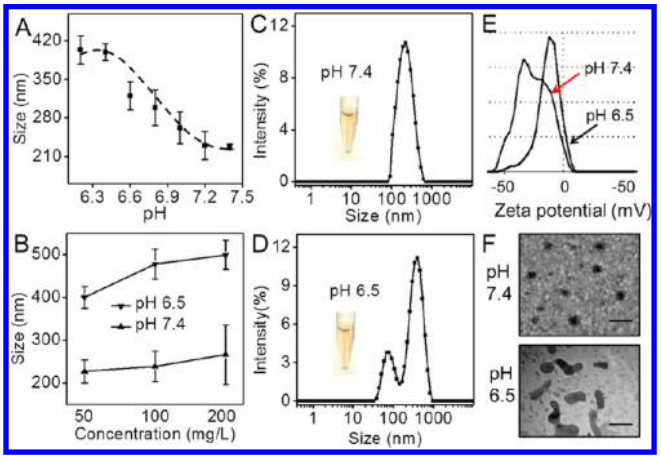

Figure 2. (A) Size titration curve of PPDT at various pH values. (B) Hydrodynamic size of PPDT at different concentrations. Hydrodynamic size of PPDT at (C) pH 7.4 and (D) pH 6.5. The inset is the images of a PPDT solution with different pH values after centrifugation. (E) ζ potentials of PPDT at pH values of 7.4 and 6.5. (F) TEM images of PPDT at pH 7.4 and 6.5. The scale bar is 300 nm.

3.2. Mild Acidity-Triggered Parameter Changes of the Chimeric Peptide. It was known that a hydrophilic carboxylate anion existed in PPDT at physiological pH, while at mildly acidic environment, a hydrophilic carboxylate anion got protonated to form a hydrophobic carboxyl group,[23−28] which would increase the hydrophobicity and hydrodynamic size of PPDT. The size titration curve at different pHs demonstrated that the hydrodynamic size of PPDT would gradually increase with decreasing pH (Figure 2A). A platform appeared around pH 6.5. Meanwhile, PPDT performed well stability at pH values of 7.4 and 6.5 regardless of the increasing concentration (Figure 2B). Specifically, the dynamic light scattering (DLS) results of PPDT in a PBS buffer revealed that a sharp peak around 220 nm was found at pH 7.4 (Figure 2C), while a dual peak appeared at pH 6.5 (Figure 2D), suggesting different self-assembly behaviors between pH 7.4 and 6.5. The hydrodynamic size change at a function of time revealed that PPDT had a very short pH response time, which was less than 10 min (Figure S3A). Meanwhile, PPDT exhibited well stability at pH values of 7.4 and 6.5 (Figure S3A,B). In addition, this protonation behavior also verified that the ζ potentials of PPDT were −26.0 ± 1.2 and −7.8 ± 0.6 mV at pH 7.4 and 6.5, respectively (Figure 2E).

In order to gain insight of the self-assembly behavior, the morphology of PPDT at pH values of 7.4 and 6.5 was observed via TEM. PPDT could self-assemble into spherical nanoparticles at pH 7.4 (Figure 2F). TPE and PpIX formed a hydrophobic core, and the deprotonated PEG_8−RDEVDG sequence formed a hydrophilic shell. Amphiphilic PPDT with a core−shell structure formed a spherical assembly. Once PPDT was incubated at pH 6.5, a predominantly spherocylindrical structure was observed. Generally, a spherical assembly would form when $P < {}^1/_3$, while an elongated assembly such as rod or spherocylinder nanoparticles would appear when ${}^1/_3 < P < {}^1/_2$.[36,37] Clearly, protonation of a carboxylate anion at pH 6.5 could increase the hydrophobicity of PPDT as well as the corresponding P value, which drove the sphere-to-spherocylinder switching of PPDT. This increased hydrophobicity also decreased the cmc value. Figure S4 showed that the cmc values of PPDT at pH values of 7.4 and 6.5 were 12.6 and 8.5 mg/L, respectively. Note that PPDT was not an entirely homogeneous phase at pH 6.5, containing a minor component of spherical nanoparticles, because mixed phases are common for an elongated self-assembly.[38,39] Besides, the size determined via DLS was larger than that measured via TEM because the water molecule in the self-assembly got removed in the vacuum state, leading to the shrinkage of PPDT during TEM observation.[40]

3.3. Tumor Acidity-Triggered Selective Cellular Internalization. The ζ potential and morphology of nanoparticles could significantly affect the cellular internalization.[41−44] Meanwhile, the pH in normal tissue was 7.3−7.4, and the tumor tissue exhibited mild acidity (pH 6.3−6.9) because of enhanced glycolysis and plasma membrane proton pumping. Therefore, PPDT was expected to possess a relative selectivity in cellular internalization between normal and tumor cells. Herein, culture media of pH 7.4 and 6.5 were employed to simulate a neutral physiological environment of normal tissue and a mildly acidic tumor tissue extracellular environment, respectively. Cellular internalization was conducted via CLSM. Encouragingly, strong red fluorescence of PpIX was observed at pH 6.5 (Figure 3A3), while the red fluorescence was much weaker at pH 7.4 (Figure 3B3). Quantitative analysis was further studied via flow cytometry (Figure 3C). The results

DOI: 10.1021/acsami.7b04447
ACS Appl. Mater. Interfaces 2017, 9, 16043−16053

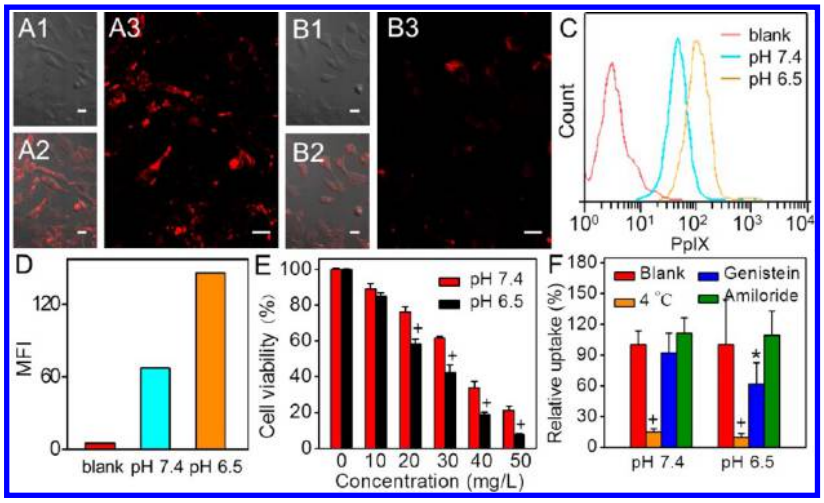

Figure 3. Cellular internalization of PPDT at (A1−A3) pH 6.5 and (B1−B3) pH 7.4. Red signal: PpIX. A1 and B1: bright field. The scale bar was 10 μm. (C) Flow cytometry analysis and (D) the corresponding MFI values of cellular internalization of PPDT at different pH values. Red line: blank control. Blue line: pH 7.4. Brown line: pH 6.5. (E) Phototoxicity of PPDT against HeLa cells at different pH values. The light irradiation time was 75 s. $^{+}p < 0.01$ when the cytotoxicity at pH 6.5 was compared with that at pH 7.4. (F) Relative uptake PPDT at pH 6.5 and 7.4. ^{+}p and $^{*}p < 0.05$ when the group was compared with the group of blank cells.

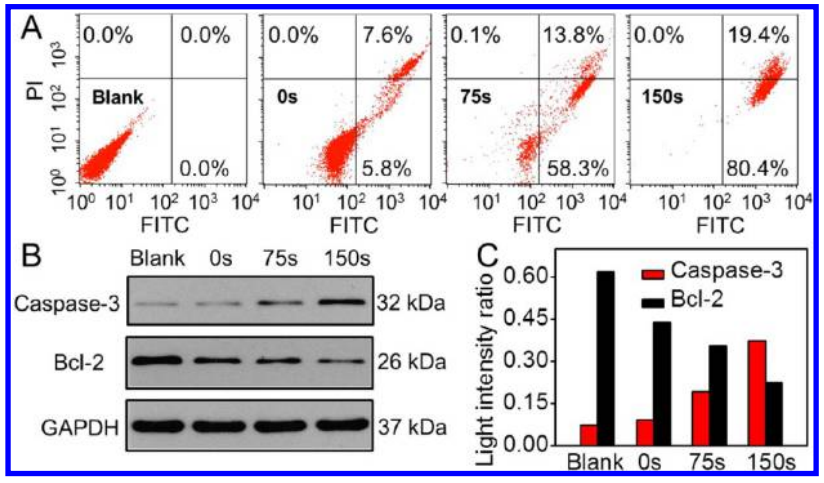

Figure 4. (A) PDT-mediated cell apoptosis with 0, 75, and 150 s of light irradiation analyzed via Annexin V-FITC/PI assay. (B) Expression of caspase-3 and Bcl-2 proteins with 0, 75, and 150 s of light irradiation via Western blotting analysis and (C) the corresponding quantitative results.

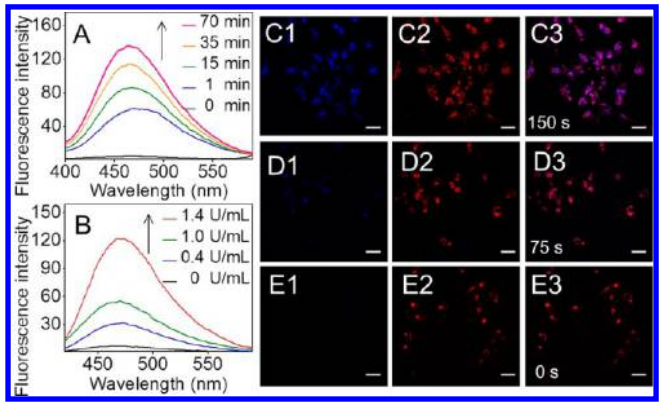

Figure 5. (A) Fluorescence spectra of PPDT (50 mg/L) when it was incubated with 1 U/mL caspase-3 enzyme with prolonged time. (B) PPDT (50 mg/L) incubated with various concentrations of caspase-3 enzyme for 1 min. CLSM images of caspase-3 enzyme responsive fluorescence recovery of TPE with various light irradiation times: (C1−C3) 150 s; (D1−D3) 75 s; (E1−E3) 0 s. The scale bar was 15 μm. Blue signal: TPE. Red signal: PpIX.

were consistent with those observed via CLSM. The intracellular fluorescence of PPDT at pH 6.5 was remarkably stronger than that at pH 7.4, when PPDT was incubated with HeLa cells for 4 h. The mean fluorescence intensity (MFI) at pH 6.5 was nearly 2-fold that at pH 7.4 (Figure 3D). All of these results substantially proved that PPDT possessed selectively enhanced internalization in acidic tumor cells; in other words, PPDT could target the tumor. Enhanced internalization was due to following facts: (1) spherocylinder-like PPDT benefited the penetration through the cell membrane due to the increased length−diameter ratio.[41−43] (2) At physiological pH, electrostatic repulsion between a negatively charged cell membrane and deprotonated PPDT severely disfavored cellular internalization.[45,46] At a mildly acidic tumor tissue, electrostatic repulsion decreased. Meanwhile, a hydrophobic carboxyl group could improve the hydrophobicity of PPDT compared with that at normal tissue. Improved hydrophobicity could increase hydrophobic interaction between PPDT and a lipid bilayer of the cell membrane, leading to accelerated cellular internalization.[47,48] The flow cytometry result further indicated that this difference in cellular

DOI: 10.1021/acsami.7b04447
ACS Appl. Mater. Interfaces 2017, 9, 16043−16053

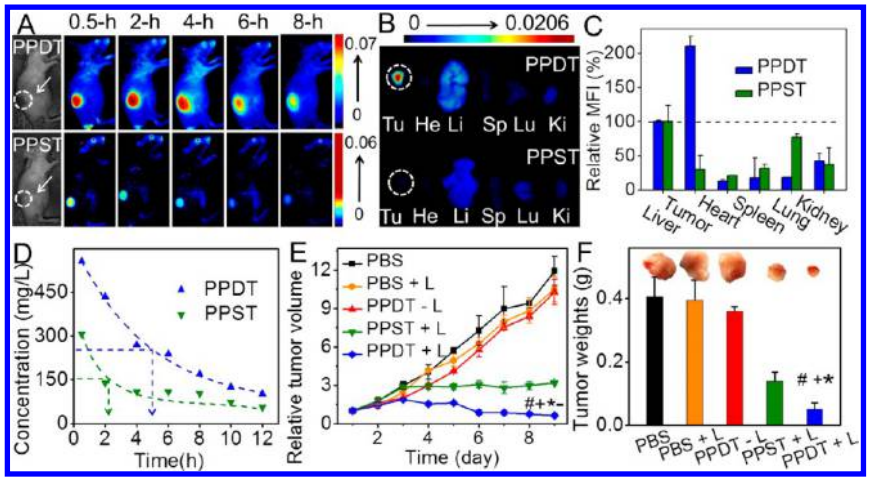

Figure 6. (A) Biodistribution images of H22 tumor-bearing mice at preset times after i.v. injection of PPDT and PPST. The white arrow pointed to the tumor tissue. The fluorescence of PpIX was used for biodistribution tracking. (B) Tumor and tissue fluorescence imaging and (C) the corresponding relative MFI values of PPDT and PPST at the 24th h after postinjection. The MFI value in the liver was set as 100% to calculate the relative MFI values. (D) Blood retention kinetic study of PPDT and PPST after i.v. injection. In vivo antitumor study via i.v. injection: (E) relative tumor volume and (F) average tumor weight of various samples. The inset was representative tumor images at the 9th day. $^{\#}p < 0.01$, $^{+}p < 0.01$, $^{-}p < 0.01$, and $^{*}p < 0.05$ when the group was compared with PBS, PBS with light irradiation, PPDT without light irradiation, and PPST with light irradiation groups, respectively. "L" means light irradiation.

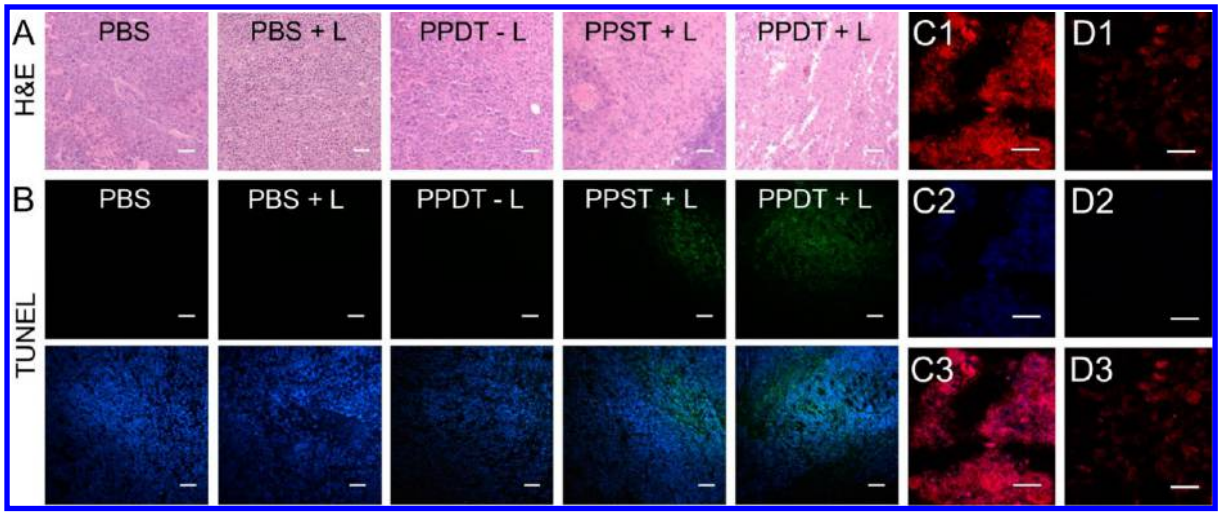

Figure 7. (A) H&E staining images and (B) TUNEL assay of H22 tumor tissues of various samples. Green signal: apoptotic cells. Blue signal: cell nucleus. The scale bar was 50 μm. In vivo apoptosis imaging of (C1−C3) PPDT with light irradiation and (D1−D3) PPST with light irradiation. Red signal: PpIX. Blue signal: TPE. The scale bar was 20 μm. "L" represents light irradiation.

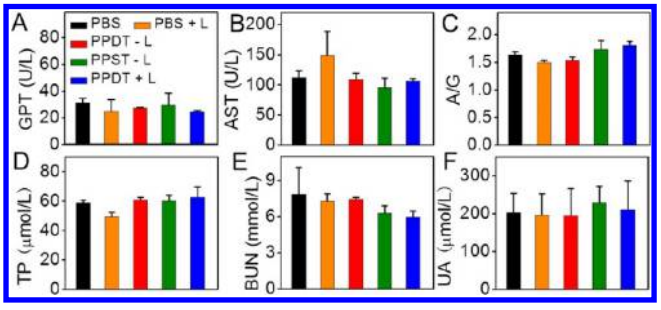

Figure 8. Serum analysis of (A) GPT, (B) AST, (C) A/G, (D) TP, (E) BUN, and (F) UA in various groups. "L" represents light irradiation.

internalization of PPDT at pH values of 7.4 and 6.5 could be observed even when PPDT was incubated with HeLa cells for 1 h, suggesting that tumor acidity-triggered selective cellular internalization was rapid (Figure S5).

Furthermore, the phototoxicity of PPDT at different pH values against HeLa cells was conducted via MTT assay. As shown in Figure 3E, PPDT at pH 6.5 with 75 s of light irradiation exhibited significantly higher cytotoxicity compared with PPDT at pH 7.4 because of the enhanced cellular internalization of PPDT in a mildly acidic environment, as confirmed above. This tumor microenvironment-triggered enhanced cellular internalization should reduce the dosage of PPDT and minimize side effects. In addition, MTT assay revealed that the phototoxicity of PPDT was irradiation-time-dependent (Figure S6). PPDT showed negligible dark toxicity due to the well biocompatibility. Also, the IC_{50} (concentration that induced 50% inhibition of cellular growth) of PPDT against HeLa cells with 75 and 150 s of light irradiation could be as low as 35 and 10 mg/L, respectively.

DOI: 10.1021/acsami.7b04447
ACS Appl. Mater. Interfaces 2017, 9, 16043−16053

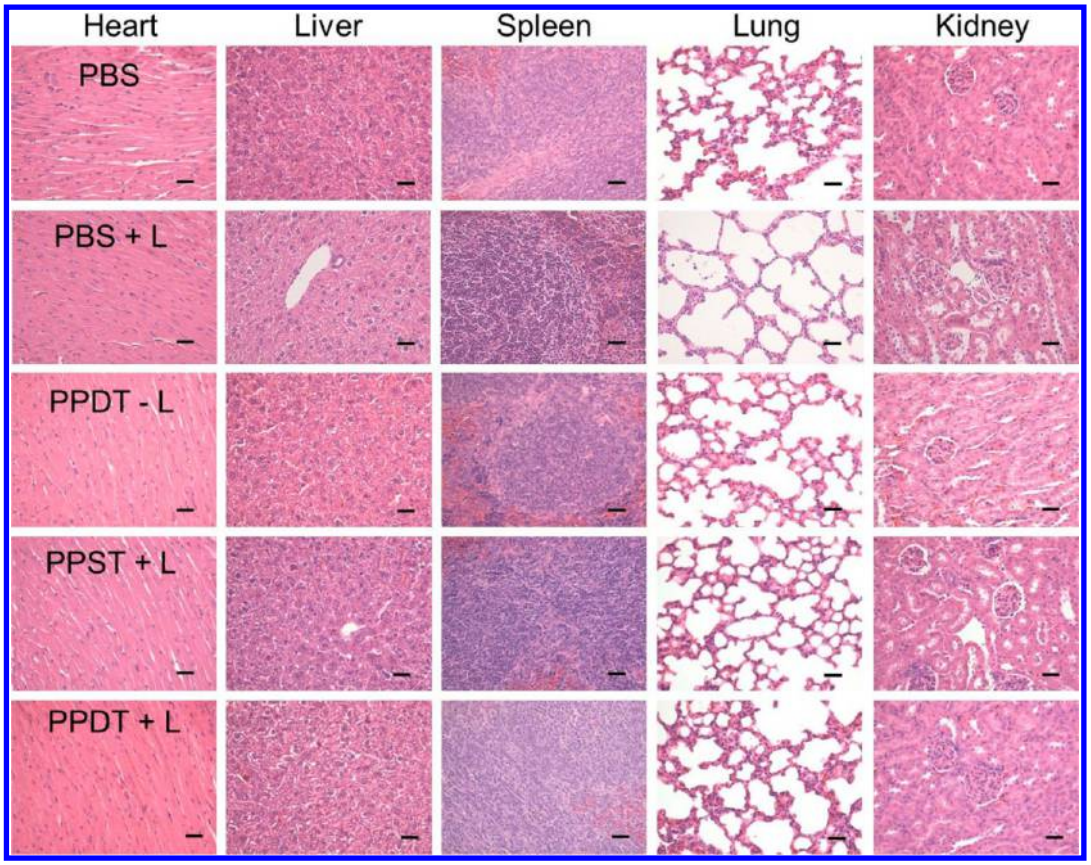

Figure 9. H&E staining images of tumor tissues of various samples. The scale bar was 50 μm. "L" represents light irradiation.

Besides, compared with the size at pH 7.4, the size of the spherocylindrical structure was larger at pH 6.5, and we further studied the cellular internalization pathway via flow cytometry. As shown in Figure 3F, the internalization of PPDT at both pH 7.4 and 6.5 was inhibited significantly, suggesting that the cellular uptake behavior was energy-dependent. Meanwhile, the introduction of endocytosis inhibitor, amiloride, would not significantly decrease the cellular internalization of PPDT at both pH 7.4 and 6.5, which indicated that PPDT was not internalized via the macropinocytosis method.[49] In contrast, the treatment of another inhibitor, genistein, dramatically decreased the internalization of PPDT at pH 6.5. This result revealed that PPDT with a spherocylindrical structure at the acidity environment underwent caveolin-mediated endocytosis.[50]

3.4. PDT-Mediated Apoptosis and AIE-Based Real-Time Therapeutic Feedback. Having established tumor selective cellular internalization and phototoxicity of PPDT, we next assessed caspase-3 enzyme responsive apoptosis imaging in vitro. Before that, PDT-mediated apoptosis was monitored by Annexin V-FITC/PI assay. As shown in Figure 4A, with prolonged light irradiation time, more cells were dead. Also, almost all cells were dead when the cells received 150 s of light irradiation. Meanwhile, 80.4% cells underwent early apoptosis with 150 s of light irradiation, suggesting that PPDT could initiate the apoptotic program during PDT. Western blotting analysis further revealed that an apoptosis biomarker caspase-3 enzyme would appear during PDT and the content of the caspase-3 enzyme increased with prolonged light irradiation time. On the contrary, PDT could inhibit the generation of antiapoptosis biomarker Bcl-2 enzyme (Figure 4B). The quantitative results were also performed in Figure 4C. Obviously, PDT-mediated apoptosis accelerated the generation of caspase-3 enzyme.

Subsequently, caspase-3 enzyme responsiveness of PPDT was conducted via the fluorescence spectrum. Figure 5A revealed that negligible fluorescence of the TPE molecule was observed in the absence of caspase-3 enzyme. When PPDT was incubated with additional caspase-3 enzyme (1 U/mL), the fluorescence signal of TPE rapidly increased with time. This fluorescence increment was due to the specific hydrolysis of the DEVDG sequence between Asp and Gly by caspase-3 enzyme.[51] The breakage of DEVDG released a hydrophobic TPE molecule, leading to restricted rotation of the phenyl groups in TPE as well as AIE.[52−54] Moreover, PPDT was mixed with various concentrations of enzyme, and the fluorescence spectra at 1 min were recorded (Figure 5B). The fluorescence signal of TPE increased faster when the concentration of caspase-3 enzyme increased, indicating that the hydrolysis rate of the DEVDG sequence was dependent on the concentration of caspase-3 enzyme.

In vitro AIE recovery of PPDT against HeLa cells was further conducted via CLSM to evaluate apoptosis imaging efficacy. Different irradiation times were performed. As shown in Figure 5E1,E2, the blue signal in HeLa cells was very weak, while an obvious red signal of PpIX was found when no irradiation was performed, suggesting PPDT could be internalized by tumor cells with low dark toxicity. When the irradiation time was prolonged, the intensity of blue fluorescence significantly increased (Figure 5C1,D1). Apparently, cell apoptosis was activated by PDT, and caspase-3 enzyme formed during this process.[55,56] Caspase-3 enzyme hydrolyzed PPDT, leading to timely AIE imaging of the TPE molecule. The AIE recovery

DOI: 10.1021/acsami.7b04447
ACS Appl. Mater. Interfaces 2017, 9, 16043−16053

during PDT was further quantitatively determined via flow cytometry (Figure S7), which was in agreement with the result observed via CLSM.

3.5. Tumor Imaging, Biodistribution, and Blood Retention Time of the Chimeric Peptide. Motivated by the excellent properties of PPDT in vitro, we proceeded to investigate the in vivo performance using an H22 tumor-bearing mouse as a model. To verify that the acidity-triggered change of the morphology switch and size enlargement in PPDT could further elevate the EPR-effect-mediated tumor accumulation, PpIX−PEG_8−RSSVSG−K(TPE)−V−$CONH_2$ (designated as PPST) was used as a negative control. Because aspartic acid and glutamic acid were replaced by neutral serine, PPST self-assembled into spherical nanoparticles and did not exhibit pH-responsive size enlargement (181.1 ± 1.4 nm at pH 6.5 and 179.5 ± 1.5 nm at pH 7.4; Figure S8A1,B1) and morphology switch (Figure S8A2,B2). As shown in Figure 6A, PPDT accumulated superfast in the tumor tissue with high efficacy just within 0.5 h and the fluorescence intensity remained instant even at the 4th h. In sharp contrast, the fluorescence of PPST was relatively low and decreased very rapidly, and the signal was almost negligible at the 6th h. These remarkable differences were mainly due to a tumor acidic environment-triggered sphere-to-spherocylinder morphology switch and subsequent size enlargement, which successfully restricted free diffusion of PPDT in a leaky vasculature network, realizing prolonged accumulation of PPDT in the tumor region. Meanwhile, tumor acidity could also specifically enhance cellular internalization of PPDT in tumor cells as proved above, which would further increase retention in the tumor region. Especially, different from traditional nanoscale drug-delivery systems in which drugs were always distributed in the whole body especially at the early stage after i.v. injection, PPDT exhibited a significantly high signal/noise ratio of the fluorescence signal in the tumor even at the 0.5th h. This superfast and efficient accumulation was attributed to rapid protonation of a carboxylate anion. None of the chemical structures need to be broken during this process, which resulted in a superfast morphology switch and size enlargement in the tumor region compared with the enzyme- or redox-responsive systems.

Thereafter, fluorescence in the tumor and other organs was observed after mice were sacrificed at the 24th h. As shown in Figure 6B, a strong fluorescence signal was observed in the tumor in the PPDT group, which was even much stronger than that in the main metabolic organs liver and kidney, while in the PPST group, the strongest signal of PPST appeared in the liver. The fluorescence signal in the tumor was even similar to that in the spleen. Furthermore, a quantitatively relative MFI value was calculated, and the MFI value in the liver was chosen as the internal reference to avoid a metabolic clearance-mediated negative impact upon comparison of tumor accumulation. Figure 6C revealed that the amount of PPDT in the tumor tissue was more than 2-fold that in the liver, and the amount of PPST in the tumor is only 29% that in the liver. These results further indicated excellent tumor accumulation of PPDT in the tumor. Furthermore, a pharmacokinetic study was performed in Figure 6D. The blood retention time of PPDT was higher than that of PPST, which demonstrated the fluorescence background in PPDT during in vivo imaging in Figure 6A. Clearly, well tumor accumulation and morphology switch decreased the metabolic clearance.

3.6. In Vivo PDT, Apoptosis Imaging, and Systemic Toxicity. Encouraged by well tumor-specific accumulation and internalization of PPDT, PDT efficacy in vivo was further conducted. As shown in Figure 6E, PBS, PBS with light irradiation, and PPDT without light irradiation could not inhibit tumor growth. However, tumor growth was significantly retarded by PPDT or PPST with light irradiation. Meanwhile, the relative tumor volume in the PPDT group with light irradiation was obviously smaller than that of the PPST group with light irradiation because of enhanced tumor accumulation/internalization of PPDT in the tumor tissue. After therapy was finished, tumors were collected. Representative tumor images are given in Figure 6F. The results of the average tumor weight are in agreement with that of the relative tumor volume. Subsequently, physiological morphology of the tumor tissue was observed via H&E staining to further evaluate the therapeutic effect. As shown in Figure 7A, tumor cells in PBS, PBS with light irradiation, and PPDT without light irradiation groups are dense. On the contrary, massive nuclei absence appeared in the PPDT group with light irradiation, indicating that great tumor cells were dead during PDT.[57] All of these results substantively demonstrated that improved tumor accumulation/internalization and prolonged blood circulation maximized the PDT efficacy of PPDT in vivo.

Furthermore, the mechanism of tumor inhibition was investigated via terminal deoxynucleoitidyl transferase mediated nick end labeling (TUNEL) assay. Figure 7B demonstrated that most of the cells were apoptotic in the PPDT group with light irradiation compared with other groups. To confirm that PPDT could give timely feedback simultaneously, CLSM against the tumor tissue was conducted. As shown in Figure 7C,D, the red signal of PpIX is observed in both the PPDT and PPST groups and the signal in the PPDT group is stronger than that in the PPST group, suggesting that, although PPDT and PPST could accumulate in the tumor, PPDT with a spherocylindrical shape exhibited higher efficacy of tumor accumulation/internalization. Besides, the blue signal of TPE in the PPST group was negligible, while a strong blue fluorescence was observed in the PPDT group. Clearly, PPDT could initiate cell apoptosis in vivo. The emergence of caspase-3 enzyme could specifically cleave the DEVDG sequence but not the SSVSG sequence, leading to AIE-based apoptosis imaging in vivo.

In order to evaluate the potential systemic toxicity, the survival rate and relative body weight of mice treated with a PPDT or PPST group with light irradiation was measured. No obvious change of the body weight was found (Figure S9A), and no mice died in all groups during treatment (Figure S9B), indicating that PPDT and PPST had almost no systemic phototoxicity. Besides, because the liver and kidney were primary organs for metabolism, various liver/kidney-damage-associated physiological indexes were tested to assess potential liver/kidney dysfunction.[58] There were negligible differences among various groups in the expression level of liver function markers including glutamic pyruvate transaminase (GPT; Figure 8A), aspartate aminotransferase (AST; Figure 8B), albumin/globulin ratio (A/G; Figure 8C), and total protein (TP; Figure 8D) and kidney function markers including blood urea nitrogen (BUN; Figure 8E) and uric acid (UA; Figure 8F) in serum. These physiological indexes suggested that laser irradiation would not damage the tissues. Meanwhile, although PPDT could appear in the liver and kidney during circulation, PDT of PPDT would not damage them because of the active tumor accumulation of PPDT as well as the local therapy

DOI: 10.1021/acsami.7b04447
ACS Appl. Mater. Interfaces 2017, 9, 16043−16053

property of PDT. Furthermore, the physiological morphology of organs including liver, heart, lung, spleen, and kidney after various treatments was observed via H&E staining (Figure 9). No pathological changes of the tissues occurred in all samples. Taken together, acidity-responsive PPDT possessed enhanced PDT efficacy to inhibit tumor growth with negligible side effects in vivo.

4. CONCLUSION

In summary, a tumor microenvironment-responsive chimeric peptide PPDT was fabricated for enhanced PDT and real-time AIE-based apoptosis imaging. PPDT directly took advantage of the acidic responsiveness of the bioactive DEVDG sequence to change the physicochemical parameters including the ζ potential, morphology, and size, realizing superfast and improved tumor accumulation, accelerated cellular internalization, prolonged blood circulation, and enhanced PDT efficacy with minimal side effects in vivo. Meanwhile, PPDT initiated cell apoptosis via PDT, and the rapid hydrolysis of PPDT by caspase-3 enzyme resulted in timely and sensitive AIE apoptosis imaging. This easy-to-fabricate PDT system demonstrated here simultaneously addressed the bottlenecks during PDT, i.e., the superfast, selective, and balanced accumulation/internalization in the tumor and the timely therapeutic response of PDT. More importantly, the strategy demonstrated here dramatically simplified the preparation of multifunctional PDT systems and reserved the versatility, which should show great potential in tumor therapy.

■ ASSOCIATED CONTENT

Supporting Information

The Supporting Information is available free of charge on the ACS Publications website at DOI: 10.1021/acsami.7b04447.

Synthesis process of PPDT, ESI-MS of PPDT, fluorescence recovery of TPE after PDT and the corresponding MFI value, hydrodynamic size and TEM imaging of PPST at pH 7.4 and 6.5, and the relative body weight of various groups after i.v. injection (PDF)

■ AUTHOR INFORMATION

Corresponding Authors

*E-mail: hank@mail.hzau.edu.cn.
*E-mail: hyhan@mail.hzau.edu.cn.

ORCID

Xian-Zheng Zhang: 0000-0001-6242-6005
He-You Han: 0000-0001-9406-0722

Notes

The authors declare no competing financial interest.

■ ACKNOWLEDGMENTS

This work was financially supported by the National Natural Science Foundation of China (Grants 51603080 and 21375043) and the Fundamental Research Funds for the Central Universities (Grant 2662015QD026). We thank the Center for Instrumental Analysis and Metrology, Institute of Virology, Chinese Academy of Sciences, for our in vivo imaging work and are grateful to Juan Min for her help in analyzing in vivo imaging data.

■ REFERENCES

(1) Idris, N. M.; Gnanasammandhan, M. K.; Zhang, J.; Ho, P. C.; Mahendran, R.; Zhang, Y. *In Vivo* Photodynamic Therapy Using Upconversion Nanoparticles as Remote-Controlled Nanotransducers. *Nat. Med.* **2012**, *18*, 1580−1585.

(2) Lucky, S. S.; Soo, K. C.; Zhang, Y. Nanoparticles in Photodynamic Therapy. *Chem. Rev.* **2015**, *115*, 1990−2042.

(3) Ge, J. C.; Lan, M. H.; Zhou, B. J.; Liu, W. M.; Guo, L.; Wang, H.; Jia, Q. Y.; Niu, G. L.; Huang, X.; Zhou, H. Y.; Meng, X. M.; Wang, P. F.; Lee, C. S.; Zhang, W. J.; Han, X. D. A Graphene Quantum Dot Photodynamic Therapy Agent with High Singlet Oxygen Generation. *Nat. Commun.* **2014**, *5*, 4596−4604.

(4) Dolmans, D. E. J. G. J.; Fukumura, D.; Jain, R. K. Photodynamic Therapy for Cancer. *Nat. Rev. Cancer* **2003**, *3*, 380−387.

(5) Zhang, L.; Lei, J. P.; Ma, F. J.; Ling, P. H.; Liu, J. T.; Ju, H. X. A Porphyrin Photosensitized Metal-Organic Framework for Cancer Cell Apoptosis and Caspase Responsive Theranostics. *Chem. Commun.* **2015**, *51*, 10831−10834.

(6) Matsumura, Y. Preclinical and Clinical Studies of NK012, an SN-38-Incorporating Polymeric Micelles, Which Is Designed Based on EPR Effect. *Adv. Drug Delivery Rev.* **2011**, *63*, 184−192.

(7) Maeda, H. Toward a Full Understanding of the EPR Effect in Primary and Metastatic Tumors as well as Issues Related to Its Heterogeneity. *Adv. Drug Delivery Rev.* **2015**, *91*, 3−6.

(8) Cun, X. L.; Chen, J. T.; Ruan, S. B.; Zhang, L.; Wan, J. Y.; He, Q.; Gao, H. L. A Novel Strategy through Combining iRGD Peptide with Tumor-Microenvironment-Responsive and Multistage Nanoparticles for Deep Tumor Penetration. *ACS Appl. Mater. Interfaces* **2015**, *7*, 27458−27466.

(9) Peer, D.; Karp, J. M.; Hong, S.; Farokhzad, O. C.; Margalit, R.; Langer, R. Nanocarriers as an Emerging Platform for Cancer Therapy. *Nat. Nanotechnol.* **2007**, *2*, 751−760.

(10) Allen, T. M.; Cullis, P. R. Drug Delivery Systems: Entering the Mainstream. *Science* **2004**, *303*, 1818−1822.

(11) Chien, M. P.; Thompson, M. P.; Barback, C. V.; Ku, T. H.; Hall, D. J.; Gianneschi, N. C. Enzyme-Directed Assembly of a Nanoparticle Probe in Tumor Tissue. *Adv. Mater.* **2013**, *25*, 3599−3604.

(12) Ji, T. J.; Zhao, Y.; Ding, Y. P.; Wang, J.; Zhao, R. F.; Lang, J. Y.; Qin, H.; Liu, X. M.; Shi, J.; Tao, N.; Qin, Z. H.; Nie, G. J.; Zhao, Y. L. Transformable Peptide Nanocarriers for Expeditious Drug Release and Effective Cancer Therapy *via* Cancer-Associated Fibroblast Activation. *Angew. Chem.* **2016**, *128*, 1062−1067.

(13) Nam, J.; Won, N.; Jin, H.; Chung, H.; Kim, S. pH-Induced Aggregation of Gold Nanoparticles for Photothermal Cancer Therapy. *J. Am. Chem. Soc.* **2009**, *131*, 13639−13645.

(14) Nguyen, M. M.; Carlini, A. S.; Chien, M. P.; Sonnenberg, S.; Luo, C.; Braden, R. L.; Osborn, K. G.; Li, Y.; Gianneschi, N. C.; Christman, K. L. Enzyme-Responsive Nanoparticles for Targeted Accumulation and Prolonged Retention in Heart Tissue after Myocardial Infarction. *Adv. Mater.* **2015**, *27*, 5547−5552.

(15) Du, J.; Tang, Y.; Lewis, A. L.; Armes, S. P. pH-Sensitive Vesicles Based on a Biocompatible Zwitterionic Diblock Copolymer. *J. Am. Chem. Soc.* **2005**, *127*, 17982−17983.

(16) Chien, M. P.; Carlini, A. S.; Hu, D.; Barback, C. V.; Rush, A. M.; Hall, D. J.; Orr, G.; Gianneschi, N. C. Enzyme-Directed Assembly of Nanoparticles in Tumors Monitored by *in Vivo* Whole Animal Imaging and *ex Vivo* Super-Resolution Fluorescence Imaging. *J. Am. Chem. Soc.* **2013**, *135*, 18710−18713.

(17) Dreher, M. R.; Simnick, A. J.; Fischer, K.; Smith, R. J.; Patel, A.; Schmidt, M.; Chilkoti, A. Temperature Triggered Self-Assembly of Polypeptides into Multivalent Spherical Micelles. *J. Am. Chem. Soc.* **2008**, *130*, 687−694.

(18) Min, Y.; Li, J.; Liu, F.; Yeow, E. K. L.; Xing, B. G. Near-Infrared Light-Mediated Photoactivation of a Platinum Antitumor Prodrug and Simultaneous Cellular Apoptosis Imaging by Upconversion-Luminescent Nanoparticles. *Angew. Chem., Int. Ed.* **2014**, *53*, 1012−1016.

(19) Oishi, M.; Tamura, A.; Nakamura, T.; Nagasaki, Y. A Smart Nanoprobe Based On Fluorescence-Quenching PEGylated Nanogels

DOI: 10.1021/acsami.7b04447
ACS Appl. Mater. Interfaces 2017, 9, 16043−16053

Containing Gold Nanoparticles for Monitoring the Response to Cancer Therapy. *Adv. Funct. Mater.* **2009**, *19*, 827−834.
(20) Zhen, Z.; Tang, W.; Chuang, J.; Todd, T.; Zhang, W.; Lin, X.; Niu, G.; Liu, G.; Wang, L.; Pan, Z.; Chen, X.; Xie, J. Tumor Vasculature Targeted Photodynamic Therapy for Enhanced Delivery of Nanoparticles. *ACS Nano* **2014**, *8*, 6004−6013.
(21) Huang, Y.; Qiu, F.; Shen, L. Y.; Chen, D.; Su, Y.; Yang, C.; Li, B.; Yan, D. Y.; Zhu, X. Y. Combining Two-Photon-Activated Fluorescence Resonance Energy Transfer and Near-Infrared Photothermal Effect of Unimolecular Micelles for Enhanced Photodynamic Therapy. *ACS Nano* **2016**, *10*, 10489−10499.
(22) Li, S. Y.; Cheng, H.; Xie, B. R.; Qiu, W. X.; Song, L. L.; Zhuo, R. X.; Zhang, X. Z. A Ratiometric Theranostic Probe for Tumor Targeting Therapy and Self-Therapeutic Monitoring. *Biomaterials* **2016**, *104*, 297−309.
(23) Ghosh, A.; Haverick, M.; Stump, K.; Yang, X.; Tweedle, M. F.; Goldberger, J. E. Fine-Tuning the pH Trigger of Self-Assembly. *J. Am. Chem. Soc.* **2012**, *134*, 3647−3650.
(24) Wang, S.; Huang, P.; Chen, X. Y. Hierarchical Targeting Strategy for Enhanced Tumor Tissue Accumulation/Retention and Cellular Internalization. *Adv. Mater.* **2016**, *28*, 7340−7364.
(25) Wang, Z.; Ma, G. L.; Zhang, J.; Yuan, Z. F.; Wang, L. G.; Bernards, M.; Chen, S. F. Surface Protonation/Deprotonation Controlled Instant Affinity Switch of Nano Drug Vehicle (NDV) for pH Triggered Tumor Cell Targeting. *Biomaterials* **2015**, *62*, 116−127.
(26) Liu, X. S.; Chen, Y. J.; Li, H.; Huang, N.; Jin, Q.; Ren, K. F.; Ji, J. Enhanced Retention and Cellular Uptake of Nanoparticles in Tumors by Controlling Their Aggregation Behavior. *ACS Nano* **2013**, *7*, 6244−6257.
(27) Wang, S.; Teng, Z.; Huang, P.; Liu, D.; Liu, Y.; Tian, Y.; Sun, J.; Li, Y.; Ju, H.; Chen, X.; Lu, G. Reversibly Extracellular pH Controlled Cellular Uptake and Photothermal Therapy by PEGylated Mixed-Charge Gold Nanostars. *Small* **2015**, *11*, 1801−1810.
(28) Huang, Y.; Tang, Z. H.; Zhang, X. F.; Yu, H. Y.; Sun, H.; Pang, X.; Chen, X. S. pH-Triggered Charge-Reversal Polypeptide Nanoparticles for Cisplatin Delivery: Preparation and in Vitro Evaluation. *Biomacromolecules* **2013**, *14*, 2023−2032.
(29) Zhang, C. Q.; Jin, S. B.; Li, S. L.; Xue, X. D.; Liu, J.; Huang, Y.; Jiang, Y. G.; Chen, W. Q.; Zou, G. Z.; Liang, X. J. Imaging Intracellular Anticancer Drug Delivery by Self-Assembly Micelles with Aggregation-Induced Emission (AIE Micelles). *ACS Appl. Mater. Interfaces* **2014**, *6*, 5212−5220.
(30) Cao, F. Y.; Yin, W. N.; Fan, J. X.; Tao, L.; Qin, S. Y.; Zhuo, R. X.; Zhang, X. Z. Evaluating the Effects of Charged Oligopeptide Motifs Coupled with RGD on Osteogenic Differentiation of Mesenchymal Stem Cells. *ACS Appl. Mater. Interfaces* **2015**, *7*, 6698−6705.
(31) Chen, S.; Rong, L.; Lei, Q.; Cao, P. X.; Qin, S. Y.; Zheng, D. W.; Jia, H. Z.; Zhu, J. Y.; Cheng, S. X.; Zhuo, R. X.; Zhang, X. Z. A Surface Charge-Switchable and Folate Modified System for Co-Delivery of Proapoptosis Peptide and p53 Plasmid in Cancer Therapy. *Biomaterials* **2016**, *77*, 149−163.
(32) Han, K.; Zhang, J.; Zhang, W. Y.; Wang, S. B.; Xu, L. M.; Zhang, C.; Zhang, X. Z.; Han, H. Y. Tumor-Triggered Geometrical Shape Switch of Chimeric Peptide for Enhanced *in Vivo* Tumor Internalization and Photodynamic Therapy. *ACS Nano* **2017**, *11*, 3178−3188.
(33) Han, K.; Lei, Q.; Wang, S. B.; Hu, J. J.; Qiu, W. X.; Zhu, J. Y.; Yin, W. N.; Luo, X.; Zhang, X. Z. Dual-Stage-Light-Guided Tumor Inhibition by Mitochondria-Targeted Photodynamic Therapy. *Adv. Funct. Mater.* **2015**, *25*, 2961−2971.
(34) Han, K.; Zhu, J. Y.; Jia, H. Z.; Wang, S. B.; Li, S. Y.; Zhang, X. Z.; Han, H. Y. Mitochondria-Targeted Chimeric Peptide for Trinitarian Overcoming of Drug Resistance. *ACS Appl. Mater. Interfaces* **2016**, *8*, 25060−25068.
(35) Castano, A. P.; Demidova, T. N.; Hamblin, M. R. Mechanisms in Photodynamic Therapy: Part One-Photosensitizers, Photochemistry and Cellular Localization. *Photodiagn. Photodyn. Ther.* **2004**, *1*, 279−293.
(36) Canning, S. L.; Smith, G. N.; Armes, S. P. A Critical Appraisal of RAFT-Mediated Polymerization-Induced Self-Assembly. *Macromolecules* **2016**, *49*, 1985−2001.
(37) Mai, Y. Y.; Eisenberg, A. Self-Assembly of Block Copolymers. *Chem. Soc. Rev.* **2012**, *41*, 5969−5985.
(38) Blanazs, A.; Madsen, J.; Battaglia, G.; Ryan, A. J.; Armes, S. P. Mechanistic Insights for Block Copolymer Morphologies: How Do Worms Form Vesicles? *J. Am. Chem. Soc.* **2011**, *133*, 16581−16587.
(39) Randolph, L. M.; LeGuyader, C. L. M.; Hahn, M. E.; Andolina, C. M.; Patterson, J. P.; Mattrey, R. F.; Millstone, J. E.; Botta, M.; Scadeng, M.; Gianneschi, N. C. Polymeric Gd-DOTA Amphiphiles Form Spherical and Fibril-Shaped Nanoparticle MRI Contrast Agents. *Chem. Sci.* **2016**, *7*, 4230−4236.
(40) Chen, J. X.; Wang, H. Y.; Li, C.; Han, K.; Zhang, X. Z.; Zhuo, R. X. Construction of Surfactant-Like Tetra-tail Amphiphilic Peptide with RGD Ligand for Encapsulation of Porphyrin for Photodynamic Therapy. *Biomaterials* **2011**, *32*, 1678−1684.
(41) Li, D.; Tang, Z. M.; Gao, Y. Q.; Sun, H. L.; Zhou, S. B. A Bio-Inspired Rod-Shaped Nanoplatform for Strongly Infecting Tumor Cells and Enhancing the Delivery Efficiency of Anticancer Drugs. *Adv. Funct. Mater.* **2016**, *26*, 66−79.
(42) Alemdaroglu, F. E.; Alemdaroglu, N. C.; Langguth, P.; Herrmann, A. Cellular Uptake of DNA Block Copolymer Micelles with Different Shapes. *Macromol. Rapid Commun.* **2008**, *29*, 326−329.
(43) Tree-Udom, T.; Seemork, J.; Shigyou, K.; Hamada, T.; Sangphech, N.; Palaga, T.; Insin, N.; Pan-In, P.; Wanichwecharungruang, S. Shape Effect on Particle-Lipid Bilayer Membrane Association, Cellular Uptake, and Cytotoxicity. *ACS Appl. Mater. Interfaces* **2015**, *7*, 23993−24000.
(44) Geng, Y.; Dalhaimer, P.; Cai, S. S.; Tsai, R.; Tewari, M.; Minko, T.; Discher, D. E. Shape Effects of Filaments versus Spherical Particles in Flow and Drug Delivery. *Nat. Nanotechnol.* **2007**, *2*, 249−255.
(45) Han, K.; Zhang, W. Y.; Zhang, J.; Lei, Q.; Wang, S. B.; Liu, J. W.; Zhang, X. Z.; Han, H. Y. Acidity-Triggered Tumor-Targeted Chimeric Peptide for Enhanced Intra-Nuclear Photodynamic Therapy. *Adv. Funct. Mater.* **2016**, *26*, 4351−4361.
(46) Li, F.; Chen, W. L.; You, B. G.; Liu, Y.; Yang, S. D.; Yuan, Z. Q.; Zhu, W. J.; Li, J. Z.; Qu, C. X.; Zhou, Y. J.; Zhou, X. F.; Liu, C.; Zhang, X. N. Enhanced Cellular Internalization and On-Demand Intracellular Release of Doxorubicin by Stepwise pH-/Reduction-Responsive Nanoparticles. *ACS Appl. Mater. Interfaces* **2016**, *8*, 32146−32158.
(47) Folk, D. S.; Torosian, J. C.; Hwang, S.; McCafferty, D. G.; Franz, K. J. Monitoring β-Secretase Activity in Living Cells with a Membrane-Anchored FRET Probe. *Angew. Chem., Int. Ed.* **2012**, *51*, 10795−10799.
(48) Liu, Z.; Zhang, Z.; Zhou, C.; Jiao, Y. Hydrophobic Modifications of Cationic Polymers for Gene Delivery. *Prog. Polym. Sci.* **2010**, *35*, 1144−1162.
(49) Zhao, D.; Xu, J. Q.; Yi, X. Q.; Zhang, Q.; Cheng, S. X.; Zhuo, R. X.; Li, F. Li F. pH-Activated Targeting Drug Delivery System Based on the Selective Binding of Phenylboronic Acid. *ACS Appl. Mater. Interfaces* **2016**, *8*, 14845−14854.
(50) Shen, G. Z.; Xing, R. R.; Zhang, N.; Chen, C. J.; Ma, G. H.; Yan, X. H. Interfacial Cohesion and Assembly of Bioadhesive Molecules for Design of Long-Term Stable Hydrophobic Nanodrugs toward Effective Anticancer Therapy. *ACS Nano* **2016**, *10*, 5720−5729.
(51) Li, S. Y.; Liu, L. H.; Rong, L.; Qiu, W. X.; Jia, H. Z.; Li, B.; Li, F.; Zhang, X. Z. A Dual-FRET-Based Versatile Prodrug for Real-Time Drug Release Monitoring and *In Situ* Therapeutic Efficacy Evaluation. *Adv. Funct. Mater.* **2015**, *25*, 7317−7326.
(52) Kwok, R. T. K.; Leung, C. W. T.; Lam, J. W. Y.; Tang, B. Z. Biosensing by Luminogens with Aggregation-Induced Emission Characteristics. *Chem. Soc. Rev.* **2015**, *44*, 4228−4238.
(53) Rananaware, A.; Bhosale, R. S.; Patil, H.; Al Kobaisi, M.; Abraham, A.; Shukla, R.; Bhosale, S. V.; Bhosale, S. V. Precise Aggregation-Induced Emission Enhancement *via* H^+ Sensing and Its Use in Ratiometric Detection of Intracellular pH Values. *RSC Adv.* **2014**, *4*, 59078−59082.

DOI: 10.1021/acsami.7b04447
ACS Appl. Mater. Interfaces 2017, 9, 16043−16053

(54) Zhu, Z.; Qian, J.; Zhao, X.; Qin, W.; Hu, R.; Zhang, H.; Li, D.; Xu, Z.; Tang, B. Z.; He, S. L. Stable and Size-Tunable Aggregation-Induced Emission Nanoparticles Encapsulated with Nanographene Oxide and Applications in Three-Photon Fluorescence Bioimaging. *ACS Nano* **2016**, *10*, 588−597.
(55) Wang, J. J.; Zhang, L. W.; Chen, M. L.; Gao, S.; Zhu, L. Activatable Ferritin Nanocomplex for Real-Time Monitoring of Caspase-3 Activation during Photodynamic Therapy. *ACS Appl. Mater. Interfaces* **2015**, *7*, 23248−23256.
(56) Hou, Z. Y.; Zhang, Y. X.; Deng, K. R.; Chen, Y. Y.; Li, X. J.; Deng, X. R.; Cheng, Z. Y.; Lian, H. Z.; Li, C. X.; Lin, J. UV-Emitting Upconversion-Based TiO_2 Photosensitizing Nanoplatform: Near-Infrared Light Mediated *in Vivo* Photodynamic Therapy *via* Mitochondria-Involved Apoptosis Pathway. *ACS Nano* **2015**, *9*, 2584−2599.
(57) Sun, C. Y.; Shen, S.; Xu, C. F.; Li, H. J.; Liu, Y.; Cao, Z. T.; Yang, X. Z.; Xia, J. X.; Wang, J. Tumor Acidity-Sensitive Polymeric Vector for Active Targeted siRNA Delivery. *J. Am. Chem. Soc.* **2015**, *137*, 15217−15224.
(58) Han, K.; Wang, S. B.; Lei, Q.; Zhu, J. Y.; Zhang, X. Z. Ratiometric Biosensor for Aggregation-Induced Emission-Guided Precise Photodynamic Therapy. *ACS Nano* **2015**, *9*, 10268−10277.

DOI: 10.1021/acsami.7b04447
ACS Appl. Mater. Interfaces 2017, 9, 16043−16053